Tensile and Compressive Deformation of a Short-Glass-Fiber-Reinforced Liquid Crystalline Polymer

R. K. Y. Li, S. N. Lu and C. L. Choy

Journal of Thermoplastic Composite Materials 1995 8: 304
DOI: 10.1177/089270579500800306

Tensile and Compressive Deformation of a Short-Glass-Fiber-Reinforced Liquid Crystalline Polymer

R. K. Y. Li*
Department of Physics and Materials Science
City Polytechnic of Hong Kong
Tat Chee Ave.
Kowloon, Hong Kong

S. N. Lu
Institute of Mechanics
Chinese Academy of Sciences
Beijing 100080, China

C. L. Choy
Department of Applied Physics
Hong Kong Polytechnic University
Kowloon, Hong Kong

ABSTRACT: Results of tensile and compression tests on a short-glass-fiber-reinforced thermotropic liquid crystalline polymer are presented. The effect of strain rate on the compression stress-strain characteristics has been investigated over a wide range of strain rates $\dot{\epsilon}$ between 10^{-4} and 350 s^{-1}. The low-strain-rate tests were conducted using a screw-driven universal tensile tester, while the high-strain-rate tests were carried out using the split Hopkinson pressure bar technique. The compression modulus was shown to vary with $\log_{10}(\dot{\epsilon})$ in a bilinear manner. The compression modulus is insensitive to strain rate in the low-strain-rate regime ($\dot{\epsilon} = 10^{-4} - 10^{-2}$ s^{-1}), but it increases more rapidly with $\dot{\epsilon}$ at higher $\dot{\epsilon}$. The compression strength changes linearly with $\log_{10}(\dot{\epsilon})$ over the entire strain-rate range. The fracture surfaces were examined by scanning electron microscopy.

1. INTRODUCTION

THERMOTROPIC LIQUID CRYSTALLINE polymers (LCP) are a class of high-performance engineering thermoplastics. They have attracted a lot of attention recently owing to their exceptional mechanical properties, thermal stability, chemical resistance, and flexibility in processing [1]. Chung [2] and Choy et al.

*Author to whom correspondence should be addresed.

0892-7057/95/03 0304–19 $10.00/0

[3] have shown that very high stiffness can be achieved even for extruded LCP rods of moderate draw ratios. In fact, the Young's modulus of 45.7 GPa at a draw ratio of 3 [3] well exceeds those for short-fiber-reinforced thermoplastic (SFRT) composites. The degree of chain orientation in injection-molded LCP is lower than that of extruded rods, but its tensile modulus and strength are still comparable to SFRT composites.

The distinct skin/core structure for injection-molded LCP is well known and has been studied by a number of workers. Ophir and Ide [4] identified a seven-layer structure for an injection-molded LCP by means of optical microscopy. Using the wide angle X-ray diffraction technique, they found that the molecular chains in the skin layer are highly aligned in the mold flow direction, while those in the core layer are almost randomly oriented. Weng et al. [5] studied the hierarchical structure of the layers based on SEM micrographs of the fracture surfaces. Boldizar [6] also identified a multi-layered structure in injection-molded LCP and measured the tensile strength in each layer. Thapar and Bevis [7] investigated the layered structure of an LCP by means of tensile modulus, microhardness, and WAXS patterns through the thickness of moldings for a range of processing conditions. The elastic moduli profile through the thickness direction for a 6-mm-thick LCP molding was measured by Sweeney et al. [8] using three-point bending and ultrasonic measurements. Mechanical tensile tests on different layers of LCP have recently been carried out by Zülle et al. [9], Schledjewski and Friedrich [10], and Li et al. [11].

The addition of a rigid reinforcement phase to engineering thermoplastic matrices to improve the overall mechanical performance is a well-established practice. The mechanical properties of fiber-reinforced LCP have been investigated in a number of studies [10–15]. In general, the incorporation of fiber reinforcement into LCP leads to a reduction in the degree of anisotropy and inhomogeneity [10,11,14,15].

The objective of this work is to study the deformation of short-glass-fiber-reinforced LCP under tensile and compressive loading. Furthermore, the effect of strain rate on the compression deformation of the composite is investigated using an Instron universal testing machine and the split Hopkinson pressure bar technique.

2. MATERIAL AND EXPERIMENTAL METHOD

The material studied in this work is Vectra A130 (Hoechst-Celanese Co.), which is a thermotropic liquid crystalline polymer (TLCP) containing 30 wt% short-glass fiber as reinforcement. The TLCP matrix is an aromatic copolyester that is believed to consist of *p*-hydroxybenzoic acid (HBA) and 2,6-hydroxynaphthoic acid (HNA). The material was supplied in the form of pellets and was injection molded into ASTM Type 1 tensile bars (3 mm thick and 12.3 mm wide in the central region). Two types of specimens were prepared from these standard tensile bars for tensile and compression testing.

It has been observed in our earlier work [11] and a number of related studies on fiber-reinforced LCP [9,10,13,14] that a skin/core structure exists in injection-

molded tensile bars. The skin layer has a higher degree of glass fiber alignment than the core, which is a result of the flow conditions during the mold process. The skin naturally extended around the whole cross section. So, in preparing the tensile specimens, the width of the tensile bars was trimmed down to 10 mm (± 5 mm from the central line) to leave a section in which the skin regions were located near the top and bottom surfaces. Tensile tests were carried out using an Instron model 4206 universal tensile tester. The cross-head speed used was fixed at 1 mm/min (which gave a strain rate of $\approx 1.5 \times 10^{-4}$ s^{-1}) for all tests. Strain was measured by an extensometer having a gauge length of 50 mm.

Miniature specimens were used for compression testing. Their dimensions and the way they are attached to the loading bars for both quasi-static and impact rates of loading are shown in Figure 1. For clarity, the thickness of the adhesive layers in Figure 1(b) is exaggerated. In all cases, the specimens are in good fit with the slots in the loading bars. The specimens were all cut from the central parallel-sided gauge region of the injected-molded tensile bars. Such a miniature specimen geometry is used because of the requirement for stress equilibrium within the specimen under impact rates of loading [16]. Traditional high-strain-rate compression testings used cylindrical specimen geometries [17–21], where the conditions of stress equilibrium can be easily achieved. But in considering our presently investigated material, in which a multi-layered structure exists, a specimen geometry that is representative of the layered structure would be essential.

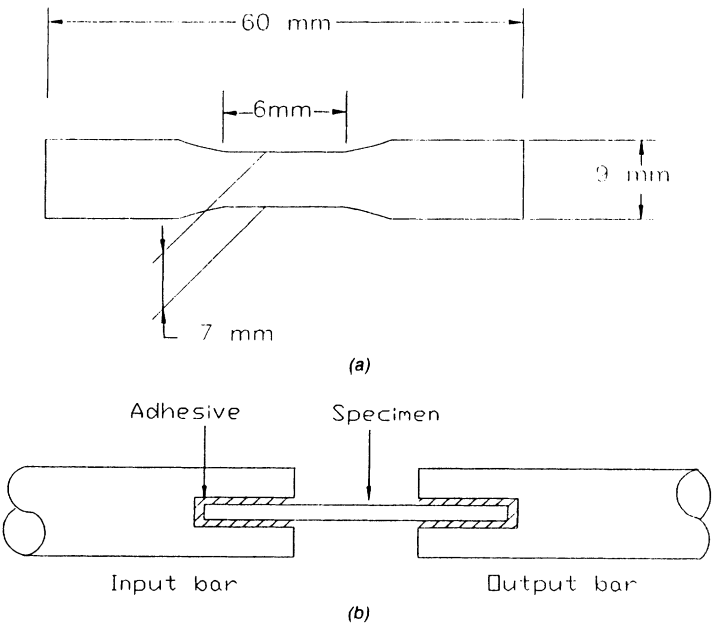

Figure 1. *(a) Specimen geometry for compression test; (b) attachment of specimen into the slotted loading bars for compression test.*

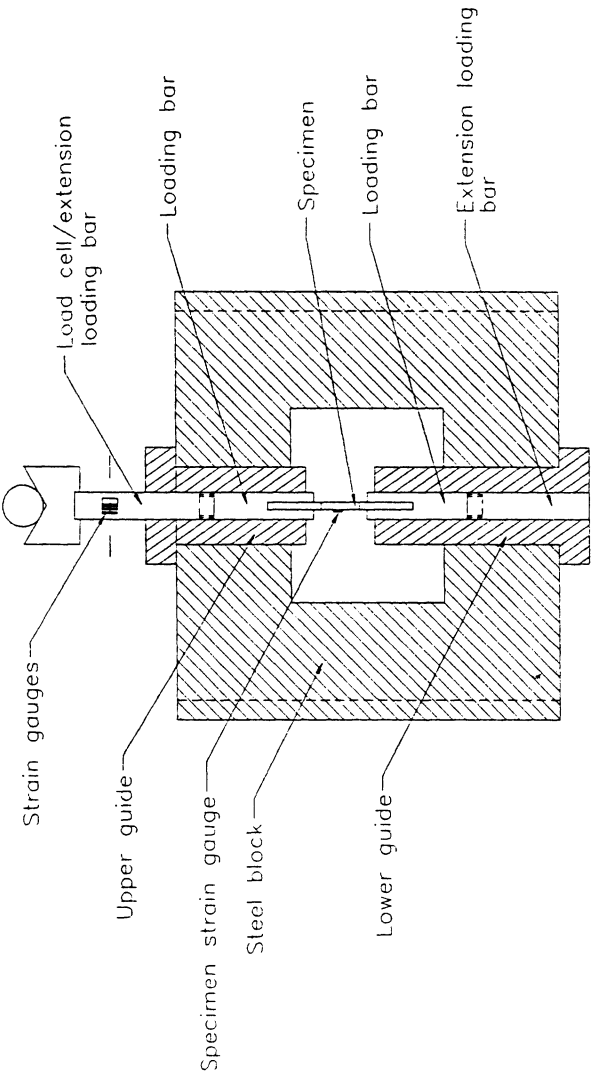

Figure 2. *Specimen support holder for low-strain-rate compression testing.*

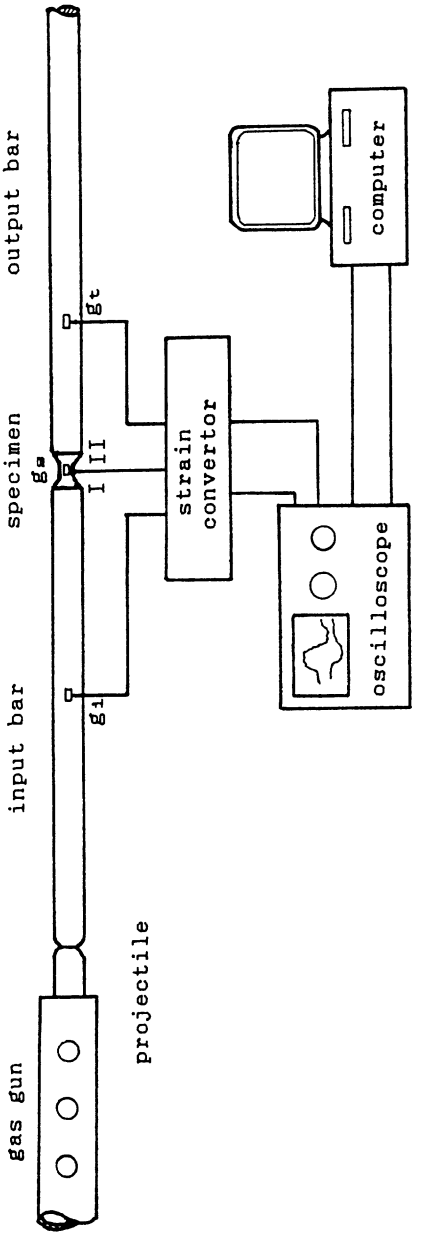

Figure 3. Compression split Hopkinson pressure bar system.

In a study of the dynamic performance of continuous-fiber-reinforced polymer composites, Harding and his co-workers [22–25] and Chiem and Liu [26] used a similar strip specimen geometry, with the specimens waisted through the thickness direction. In the present study, the specimens are waisted through the width direction.

Compression tests were carried out in two strain-rate ranges: quasi-static and impact rates of loading. Quasi-static compression was carried out using the Instron universal tester. A compression jig was developed for this purpose (Figure 2). Compression strain in the specimen gauge region was monitored using adhesively bonded strain gauges. Signals from the load cell and specimen strain gauge were fed into a strain signal conditioner and subsequently stored in a Nicolet 420 digital storage oscilloscope.

Compression testing under impact rates of loading was carried out using the split Hopkinson pressure bar (SHPB) technique. A schematic representation of the SHPB experimental setup is shown in Figure 3. Essentially, the specimen was adhesively bonded into the slotted ends of the input bar and output bar similar to the setup shown in Figure 1(b). A small gas gun was used to fire a projectile that impacted on the free end of the input bar. As in the quasi-static rate of loading, the specimen strain throughout the deformation history was measured by strain gauges bonded onto the parallel gauge region of the specimen. The stress acting on the specimen was determined from the output bar strain gauge station g_t.

The microstructural details of the composite to be considered here are the glass fiber length and the skin/core structure. The glass fiber length distribution was obtained in the following manner. First, a specimen was heated in an oven at 500°C for two hours to burn off the LCP matrix. The lengths of 500 fibers were counted using an image analyzer. The skin/core structure was examined by optical microscopy after the usual metallographic mounting and polishing procedures.

Fractographs were obtained by scanning electron microscopy (SEM-Joel JSM-820). The specimens were all gold coated before examination by SEM.

3. RESULTS AND DISCUSSION

3.1 Microstructural Details

A micrograph displaying the skin/core structure of the glass fiber/LCP composite (A130) is shown in Figure 4. The thicknesses of the two skin layers, $S1$ and $S2$, are the same. The thickness of the core layer, C, is slightly less. The ratio for the layer thickness $S1{:}C{:}S2$ is measured to be 11:10:11. The fibers in the two skin layers have a preferred orientation, which is parallel to the mold flow direction (MFD). In the core layer, the fibers are randomly oriented. The cumulative fiber length distribution is shown in Figure 5. The minimum and maximum measured fiber lengths are 0.092 mm and 0.658 mm, respectively. The mean fiber length is 0.332 mm. Since the fiber diameter is 9.3 μm, this gives an average aspect ratio of 36.

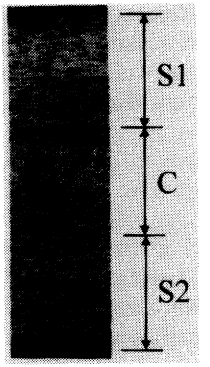

Figure 4. *Skin/core structure for an injection-molded glass fiber/LCP composite.*

3.2 Tensile Properties

Figure 6 shows the quasi-static tensile stress-strain curves of the skin, the core, and the entire A130 specimen. The skin and core specimens (each about 1 mm thick) were obtained by grinding off the unwanted materials from separate molded specimens. As can be seen, the skin specimen has the best stress-strain characteristics—i.e., it has the highest tensile modulus and tensile strength. The core specimen has the lowest, while the whole A130 specimen has intermediate values. The higher stiffness and strength values for the skin specimen can be attributed to the high degree of orientation of the LCP molecules and the glass

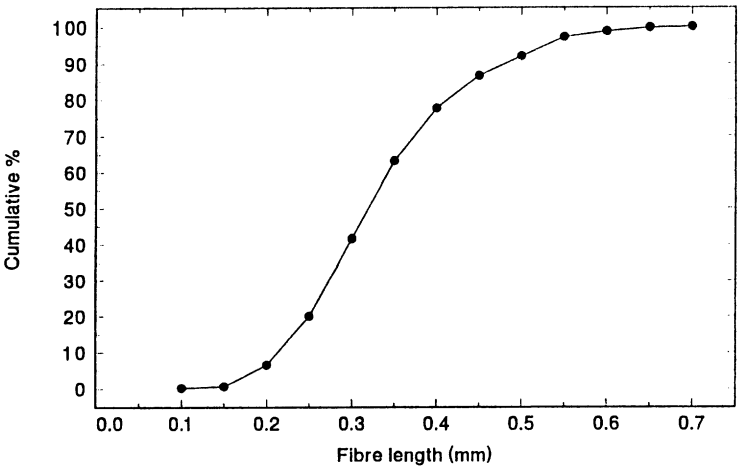

Figure 5. *Cumulative fiber length distribution for an injection-molded glass fiber/LCP composite.*

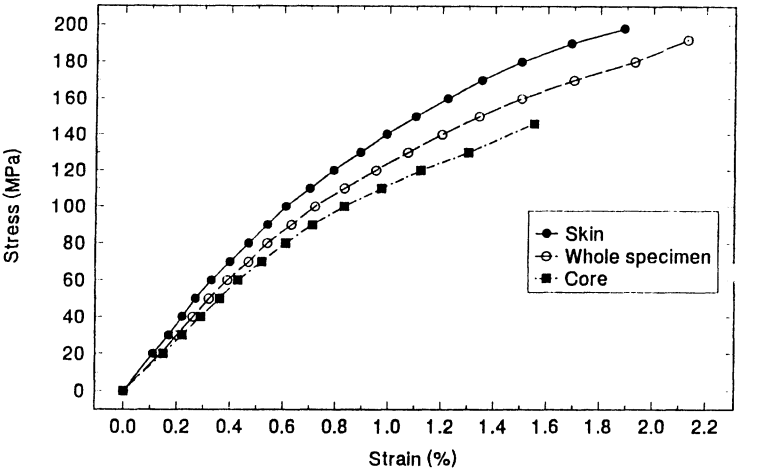

Figure 6. *Tensile stress-strain curves of various layers and of an entire sample for A130 tested at a cross-head speed of 1 mm/min.*

fibers in the skin region. Values of the Young's modulus and tensile strength for the various specimens are shown in Table 1.

In our earlier studies [11] on pure LCP (Vectra A950—which is believed to be the matrix resin for A130), the layered structure was characterized using wide angle X-ray diffraction (WAXD). It was found that injection-molded LCP A950 has two outer-true-skins (OTS), two inner-skins and a core. This outer-true-skin/inner-skin/core structure is in agreement with that proposed by Sawyer and Jaffe [27]. The tensile stress-strain curves for the various layers of A950 are shown in Figure 7 for comparison with the currently investigated A130. The OTS specimen appears to possess a very low tensile strength when compared with the others. The ease of fibrillation and thinness of the OTS specimen (about 0.1 mm thick) made it very fragile to handle. This causes the apparently low tensile strength for this layer. Comparison of Figures 6 and 7 shows that, for the whole specimen, the addition of glass fibers decreases the elongation at break (ϵ_f) from 4% to about 2%. The Young's modulus is increased from 10.8 GPa to 15.2 GPa,

Table 1. Results of tensile tests for A130 specimens.

	Young's Modulus (GPa)	Tensile Strength (MPa)
Skin	18.3	198
Core	13.3	146
Whole A130 (Measured)	15.2	192
Whole A130 (Calculated)	16.7	182

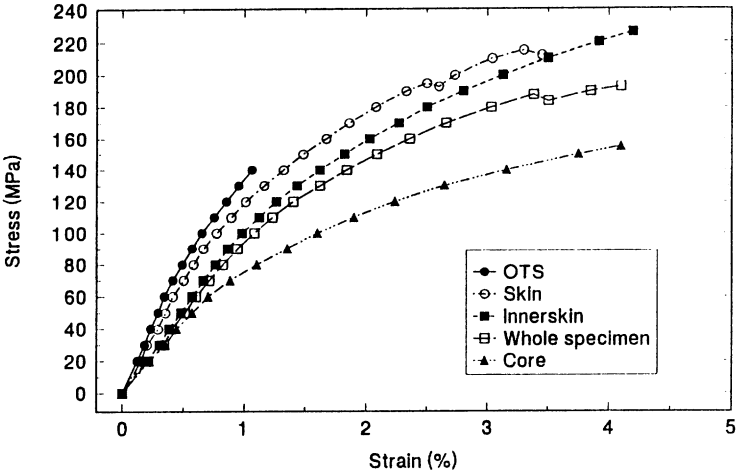

Figure 7. *Tensile stress-strain curves of various layers and of an entire sample for A950 tested at a cross-head speed of 1 mm/min.*

while the tensile strength is not significantly affected. This is in marked contrast with other engineering thermoplastics, which show an increase in strength when glass fibers are added. The insensitivity of tensile strength to the addition of 30 wt% glass fiber is in agreement with the observation of Voss and Friedrich [13].

The Young's modulus and tensile strength of the entire A130 sample can be calculated by a rule-of-mixture approach:

$$E_{whole} = \left(\frac{S1 + S2}{B}\right)E_{skin} + \left(\frac{C}{B}\right)E_{core} \tag{1}$$

$$\sigma_{whole} = \left(\frac{S1 + S2}{B}\right)\sigma_{skin} + \left(\frac{C}{B}\right)\sigma_{core} \tag{2}$$

where E is the Young's modulus, σ is the tensile strength, $S1$ and $S2$ are the thicknesses of the two skin layers, C is the core layer thickness, and B is the total specimen thickness. It is easily seen from Table 1 that the calculated values are in reasonable agreement with the observed values. The same conclusions have also been drawn on a number of filled liquid-crystal polymer systems by Schledjewski and Friedrich [10].

3.3 Compression Test Results and Strain Rate Effect

When carrying out compression testing in the present investigation, it is crucial to make sure that the deformation is uniaxial; i.e., bending of the specimens does not occur prematurely. Upon reaching large deformation, bending of the compression specimen may eventually occur, which depends on the nature of the fail-

ure mode. For brittle failure, bending will not occur. For ductile failure, bending is likely to occur on reaching the inelastic region of the stress-strain curve due to shear buckling.

The compression stress-strain curves for a specimen tested at a quasi-static rate of loading are shown in Figure 8, where the curves labelled ϵ_a and ϵ_b are strain signals obtained from the two strain gauges bonded to the opposite parallel faces of the same compression specimen. It can be seen that ϵ_a and ϵ_b give nearly identical stress-strain curves up to a strain level of about 1.2%. Beyond that strain level, either shear buckling occurs, or one of the strain gauges starts to debond from the specimen surface, so the two specimen strain gauges deviate from each other. A good correlation between ϵ_a and ϵ_b was also found for other strain rates of testing.

Compression stress-strain curves obtained at three strain rates are shown in Figure 9. A very significant influence of strain rate on the stress-strain curves can be seen. Increase in strain rate causes a corresponding increase in elastic modulus and compression strength. The variation of the Young's modulus (E_c) with log ($\dot{\epsilon}$) is shown in Figure 10. It can be seen that in the low-strain-rate regime, the Young's modulus E_c is relatively insensitive to the change in strain rate. But as the strain rate increases to above 10^{-2} s^{-1}, the strain-rate sensitivity increases, which is reflected by a slight increase in the slope of the Young's modulus E_c against log ($\dot{\epsilon}$) plot. It has to be stressed that the observed dependency between Young's modulus and strain rate is significantly temperature dependent.

The effect of strain rate, $\dot{\epsilon}$, on the compression strength, σ_c, is shown in Figure 11. The data points are more scattered, but an approximately linear relationship exists between σ_c and log ($\dot{\epsilon}$).

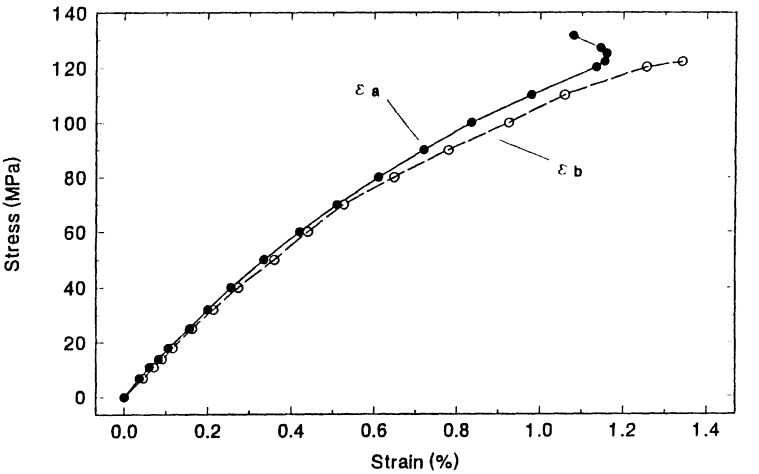

Figure 8. *Comparison of compression stress-strain curves obtained from strain gauges bonded to opposite faces of the same specimen.*

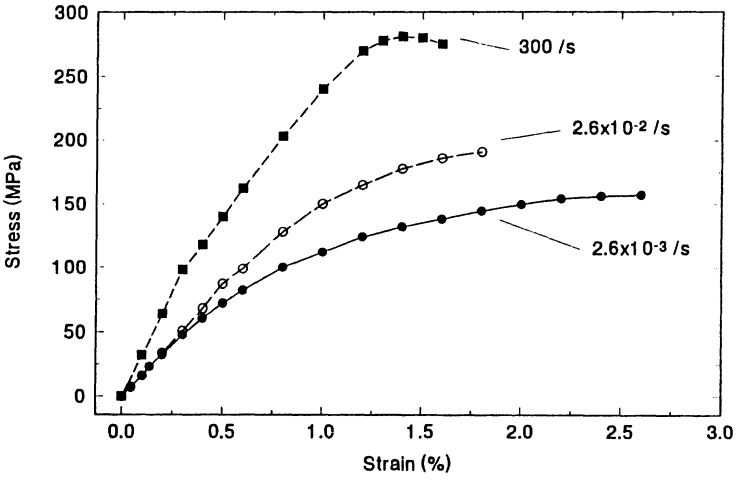

Figure 9. *Compression stress-strain curves for A130 at three different strain rates.*

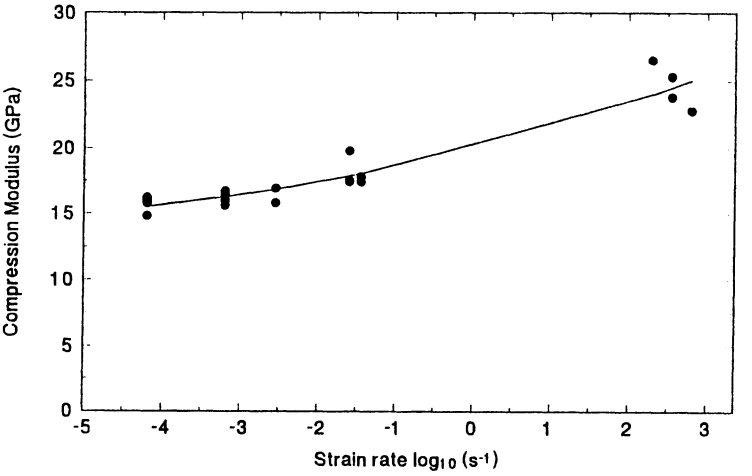

Figure 10. *Effect of strain rate on compression modulus for A130.*

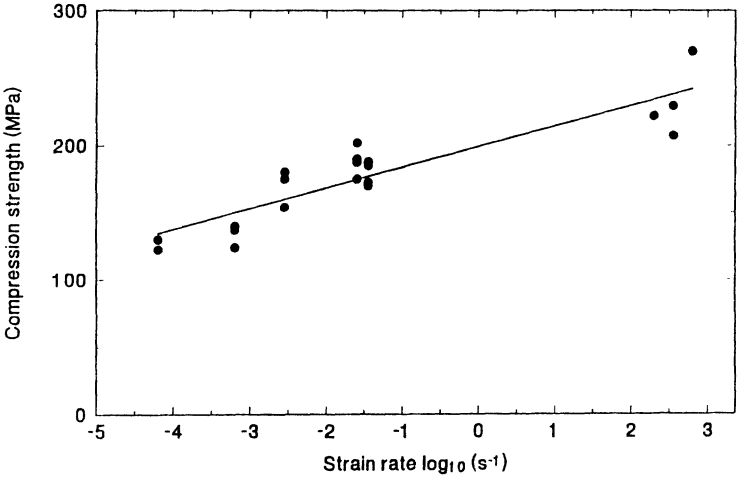

Figure 11. *Effect of strain rate on compression strength for A130.*

Representative compressive failure modes at strain rates of 10^{-3} s^{-1}, 5×10^{-2} s^{-1}, and 350 s^{-1} are shown in Figure 12. At a strain rate of 10^{-3} s^{-1}, a localized shear buckling failure mode can be seen [Figure 12(a)]. Outside the localized shear failure zone, no apparent damage can be observed visually. This type of localized shear failure mode is observed for all specimens tested and failed under low strain rates. At higher strain rates, about 5×10^{-2} s^{-1}, the damage is more spread out [Figure 12(b)]. Some delamination failure can be seen. The delamination is not unexpected because of the layer structure of LCPs. For the specimens that failed at the impact rate of loading ($\dot{\epsilon} \approx 350$ s^{-1}), the fracture mode is again different [Figure 12(c)]. The failure is catastrophic, with the specimen being broken into a number of pieces.

3.4 SEM Fractography

In this section, SEM examination of the fracture surfaces will be presented. First, the fracture surfaces for tensile specimens that failed at quasi-static rate of loading will be shown. Then, we will examine the compression specimens that failed at quasi-static and impact rate of loadings.

Figure 13(a) shows the fracture surface of an entire tensile specimen. The core and skin regions can be easily identified. The glass fibers in the core region (labelled c) can be seen to be oriented in a random fashion. In the skin region (labelled s) the fibers are well aligned parallel to the melt flow direction. In the same photograph we can also identify some of the relatively long pull-out glass fibers. Careful measurement on the tensile fracture surfaces gave a maximum glass fiber pull-out length of approximately 0.5 mm. Under axial tension, the glass fiber experiences tensile stress along its length with the maximum value

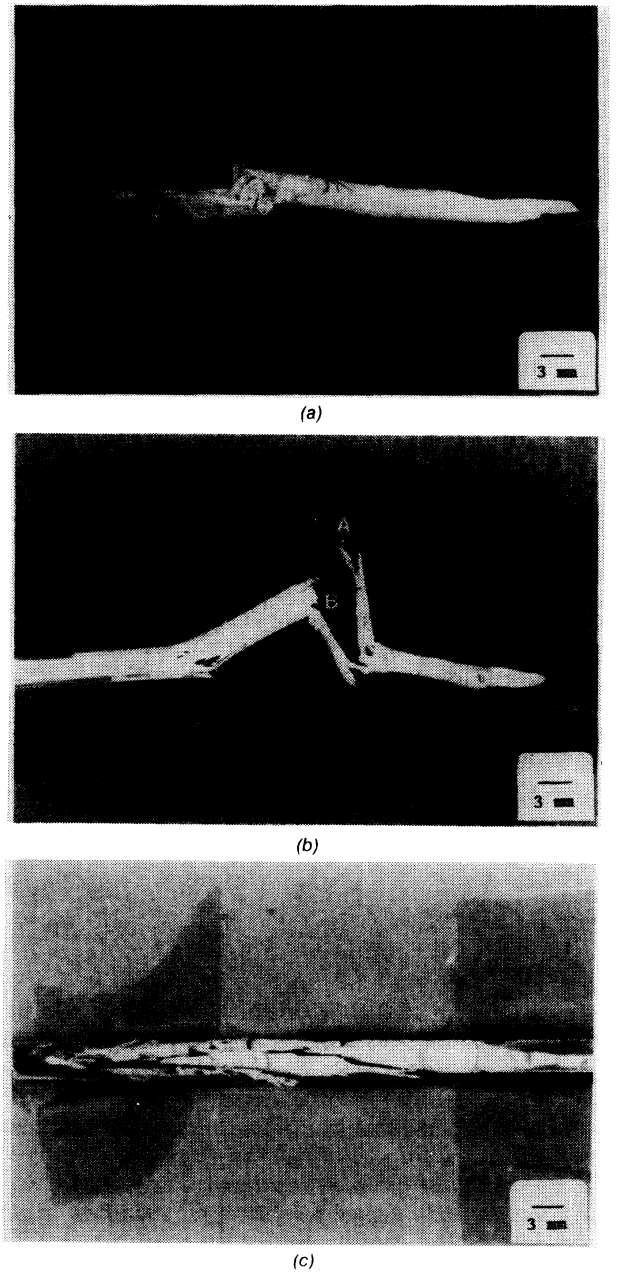

Figure 12. *Compression failure of A130 samples at various strain rates: (a) 10^{-3} s^{-1}; (b) 5×10^{-2} s^{-1}; (c) 350 s^{-1}.*

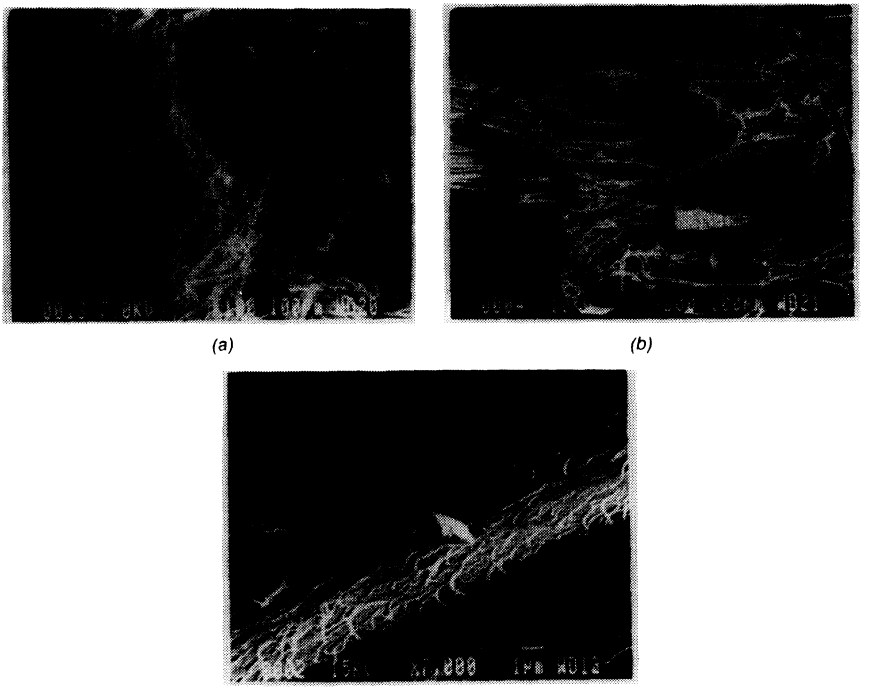

Figure 13. *Fracture surfaces of tensile samples: (a) skin and core region; (b) layered structure of the skin region; (c) LCP microfibrils on glass fiber surface.*

occurring at the central portion of the fiber, while shear stress is developed at the fiber ends. The relative magnitude of these stresses is determined by the fiber length and the interfacial bond strength. For a fiber shorter than the critical fiber length, (l_c), the tensile stress along the fiber never reaches its ultimate strength; therefore fiber pull-out is the dominant failure mechanism. For fibers longer than l_c, fiber fracture is the major failure mechanism, since the tensile stress along the fiber can now exceed the tensile strength. Therefore, the lengths of the longest fiber protruding from the tensile fracture surface provide an approximate measure of the critical fiber length; i.e., the longest protruded length should not be larger than $l_c/2$.

Our measured maximum protruded fiber length of about 0.5 mm suggests a l_c value of at least 1 mm, which exceeds the observed maximum length of the fibers (Figure 5). This implies that the fibers are not stressed to fracture. Therefore, the incorporation of glass fibers cannot improve the tensile strength, which is supported by our observation that the tensile strengths for A130 and A950 are about the same (see Figures 6 and 7).

Other than fiber orientation, the SEM micrograph also shows a distinct difference in fracture surface appearance between the skin and core regions. The

entire core region appears as a single bulk structure. In the skin region, on the other hand, the fractured material has a layer structure [Figure 13(b)]. Furthermore a number of LCP fibrils can be seen. It is expected that the tearing off of the LCP fibrils from the LCP matrix will also contribute significantly to energy absorption in the fracturing process. Figure 13(c) shows a glass fiber located in the fractured skin region of a tensile specimen. It can be seen that the glass fiber surface is covered by a high concentration of LCP microfibrils. These microfibrils, which have a diameter of about 0.1 μm, are among the basic elements of the hierarchical structural model proposed for extruded and injection-molded LCP components [27]. Evidence of the large number of microfibrils adhering to the glass fiber surface indicates a strong bonding between the LCP and glass fiber. Even though a strong bond exists between the LCP and the glass fiber, the LCP is easy to fibrillate, which results in a long critical fiber length in comparison with the glass fiber lengths.

A compression specimen that failed at a strain rate of 10^{-3} s^{-1} was sectioned longitudinally and then polished. The prepared sample is shown in Figure 14(a),

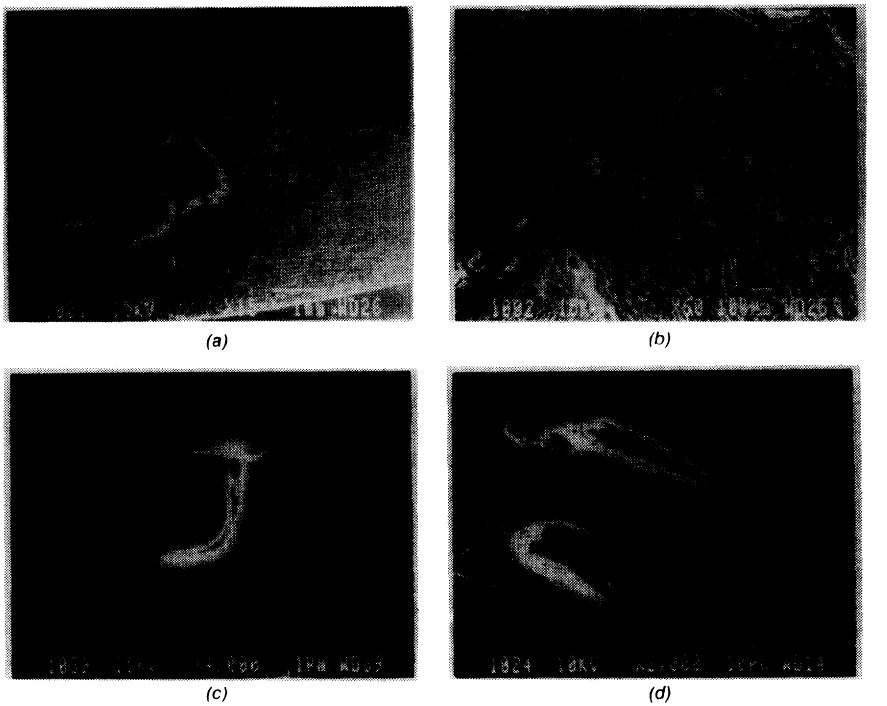

Figure 14. *Cross-sectional view of a compression sample that failed at a strain rate of 10^{-3} s^{-1}: (a) micrograph showing the formation of a large shear crack; (b) micrograph at higher magnification showing the various damage mechanisms; (c) cracking of glass fiber; (d) cracking in the matrix and at the fiber/matrix interface.*

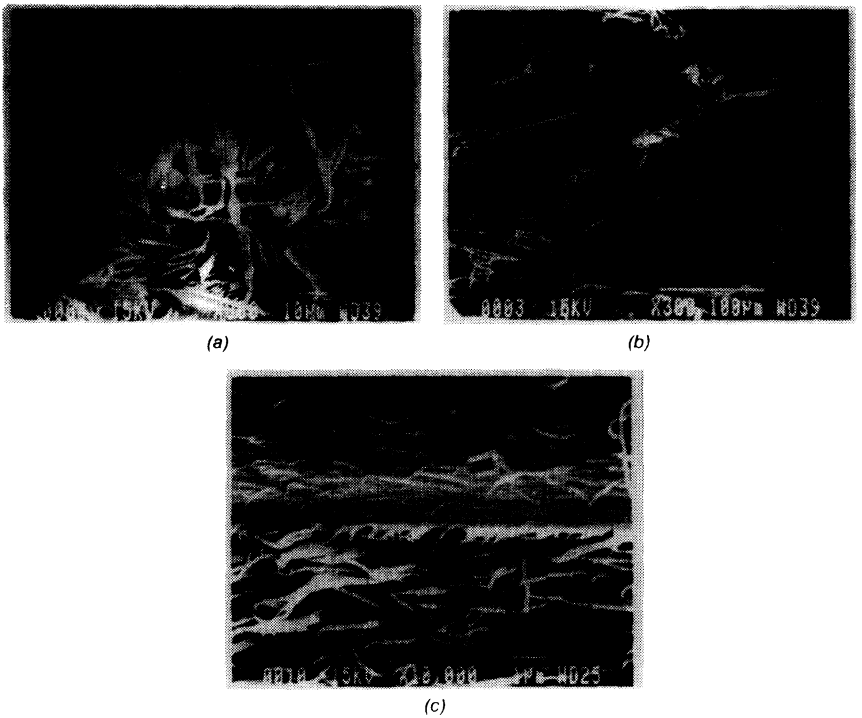

Figure 15. *Fracture surface of a compression sample tested at a strain rate of 5 × 10^{-2} s^{-1}: (a) presence of fibrils at the tearing-off region; (b) the delaminated plane has a smooth appearance; (c) microfibrils on the glass fiber surface and in the matrix.*

in which the length direction of the specimen is horizontal and the thickness direction vertical. It can be seen that the damage mode is shear buckling, and the damage zone is confined to a localized region, with a large shear crack (labelled sc) being evident. Outside this region, no apparent damage can be observed. Figure 14(b) is a magnified view of the severely damaged region in Figure 14(a). At such a damage level, it can be seen that the major damage mechanisms are elastic fiber bending, fiber fracture, fiber/matrix debonding, and matrix separation or cracking. Of course, elastic fiber bending can be seen as the precursor to fiber fracture. Figure 14(c) shows a fractured fiber embedded in an LCP matrix. It can be seen that the crack starts perpendicular to the fiber axis due to the bending stress. But instead of propagating catastrophically, the fiber crack has been deflected sideways and then arrested. Furthermore, fiber/matrix debonding can be seen near the crack initiation site. Figure 14(d) shows a region of matrix crack initiation. The upper matrix crack is seen to have initiated in the matrix while the lower matrix crack is seen to have initiated at the fiber/matrix interface.

Figure 15(a) shows the fracture surface of a compression specimen that failed at a strain rate of 5 × 10^{-2} s^{-1} [region A in Figure 12(b)]. A number of LCP

fibrillar strips (with a width of about 5 μm and a thickness much smaller than the width), together with a large number of small-diameter LCP fibrils, can be seen. Figure 15(b) shows the fracture surface corresponding to the delaminated surface (region B) in Figure 12(b). The fracture surface is very smooth, indicating fast fracture along this plane. Higher magnification of a glass fiber (labelled F) and its neighboring LCP matrix (labelled M) is shown in Figure 15(c). Similar to the previous case of the tensile specimen [Figure 13(c)], LCP microfibrils are found on the glass fiber surface and the surrounding LCP matrix.

Microscopically, there is a striking difference between low- and high-strain-rate failed specimens. As we have seen earlier, for both tensile and compression loadings at low strain rates, the protruded glass fiber surfaces are well covered with LCP in the form of microfibrils [see Figures 13(c) and 15(c)]. Figure 16 shows a glass fiber and its neighboring matrix on the fracture surface of a compression specimen that failed at a strain rate of $\approx 350\ s^{-1}$. Even though the LCP matrix is still adhering strongly to the glass fiber surface, no LCP microfibrils can be seen. Furthermore, the LCP matrix fails in a brittle manner.

As a result of the injection-molding process, there are LCP fibrils and microfibrils throughout the matrix, some of which are strongly adhering to the glass fibers. At a low rate of testing, these will remain intact and are observed on the fracture surfaces. Due to adiabatic heating during impact rate of loading, the microfibrils may have melted and therefore not been observed (Figure 16).

4. CONCLUSIONS

Tensile and compressive deformation of an injection-molded short-glass-fiber-reinforced LCP have been investigated in this work. The addition of short glass fibers into the LCP increases the tensile modulus by 50%, but the tensile strength is not significantly affected. Fractographic measurements give a critical fiber length of about 1 mm, which is longer than the maximum measured glass fiber length in the injection-molded samples. Therefore, the glass fibers cannot be stressed to their fracture strength.

Figure 16. *Absence of microfibrils on the glass fiber surface for a compression sample that failed at a strain rate of 350 s^{-1}.*

The strain-rate dependence for the compression modulus and compression strength of the composite have been determined. The compression modulus varies with $\log_{10}(\dot{\epsilon})$ in a bilinear manner, with the knee point at a strain rate of approximately 10^{-2} s^{-1}. Below the knee point, the strain-rate sensitivity is low. Above the knee point, the strain-rate dependence is slightly stronger. The compression strength varies in a linear manner with $\log_{10}(\dot{\epsilon})$ over the entire strain-rate range studied in this work.

Macroscopic inspection of the compression failed specimens showed that strain rate has a strong influence on the failure mode. Fractographic examination indicated that the tearing off of both fibrils and microfibrils from the LCP matrix contributes significantly to energy absorption during failure. The adhesion between LCP and glass fiber is strong, as indicated by the fact that all exposed glass fibers are well covered with LCP. At low tensile and compression rates of loading, the LCP adhering to the fiber surface is in the form of microfibrils. For compression specimens that failed at impact rate ($\dot{\epsilon} \approx 350$ s^{-1}), the LCP covering the fibers is not in fibrillar form. This may be because the microfibrils have melted as a result of adiabatic heating under impact loading.

ACKNOWLEDGEMENTS

This work is supported by the Hong Kong Universities and Polytechnics Grants Committee Grant No. 904-034.

REFERENCES

1. Donald, A. M. and A. H. Windle. 1992. *Liquid Crystalline Polymers.* Cambridge University Press.
2. Chung, T. S. 1988. "Production of Ultrahigh-Modulus Liquid-Crystal Polymer Rods," *J. Polym. Sci., Polym. Phys. Ed.*, 26:1549–1552.
3. Choy, C. L., W. P. Leung and A. F. Lee. 1992. "Ultrasonic Measurements of the Elastic Moduli of Liquid Crystalline Polymers," *Polymer,* 33:1788–1791.
4. Ophir, Z. and Y. Ide. 1983. "Injection Molding of Thermotropic Liquid Crystal Polymers," *Polym. Eng. Sci.*, 23:792–796.
5. Weng, T., A. Hiltner and E. Baer. 1986. "Hierarchical Structure in a Thermotropic Liquid-Crystalline Copolyester," *J. Mater. Sci.*, 21:744–750.
6. Boldizar, A. 1988. "The Effects of Injection Rate and Mould Design on the Mechanical Properties of an Injection Molded Liquid Crystalline Copolyester," *Plastics Rubber Proc. Appl.*, 10:73–78.
7. Thapar, H. and M. J. Bevis. 1989. "Processing, Property and Morphology of an Injection Moulded Liquid Crystal Thermoplastic Polymer," *Plastics Rubber Proc. Appl.*, 12:39–52.
8. Sweeney, J., B. Brew, R. A. Duckett and I. M. Ward. 1992. "Mechanical Anisotropy and Inhomogeneity of an Aromatic Liquid Crystalline Polyester," *Polymer,* 33:4901–4907.
9. Zülle, B., A. Demarmels, C. Plimmer and H. H. Kausch. 1991. "Processing, Morphology and Properties of Filled and Unfilled LCP," in *Proceedings of the 8th International Conference on Deformation Yield and Fracture of Polymers.* London: Plastic and Rubbers Institute, pp. 87/1–87/4.
10. Schledjewski, R. and K. Friedrich. 1992. "Tensile Properties of Filled Liquid-Crystal Polymer Systems," *J. Mater. Sci. Lett.*, 11:840–842.
11. Li, R. K. Y., S. N. Lu, C. L. Choy and C. McCall. 1993. "Structure-Mechanical Property

Relationship in Thermotropic Liquid Crystalline Polymer and Its Short Fiber Composite," in *Proceedings of the International Conference on Advanced Composites Fabrication, Processing, Properties, Performance, Design and Applications.* TMS, pp. 855–860.

12. Chung, T. S. and P. E. McMahon. 1986. "Thermotropic Polyester Amide-Carbon Fiber Composites," *J. Appl. Polym. Sci.*, 31:965–977.
13. Voss, H. and K. Friedrich. 1986. "Influence of Short-Fibre Reinforcement on the Fracture Behavior of a Bulk Liquid Crystal Polymer," *J. Mater. Sci.*, 21:2889–2900.
14. Wu, J. S., K. Friedrich and M. Grosso. 1989. "Impact Behavior of Short Fibre/Liquid Crystal Polymer Composites," *Composites*, 20:223–233.
15. Chivers, R. A. and D. R. Moore. 1991. "The Influence of Flow Path Length on the Stiffness and Toughness of Some Engineering Thermoplastics," *Polymer*, 32:2190–2198.
16. Harding, J. 1993. "Effect of Strain Rate and Specimen Geometry on the Compressive Strength of Woven Glass-Reinforced Epoxy Laminates," *Composites*, 24:323–332.
17. Kolsky, H. 1949. "An Investigation of the Mechanical Properties of Materials at Very High Rates of Loading," *Proc. Phys. Soc., Section B*, 62:676–700.
18. Davies, E. D. H. and S. C. Hunter. 1963. "The Dynamic Compression Testing of Solids by the Method of the Split Hopkinson Pressure Bar," *J. Mech. Phys. Solids*, 11:155–179.
19. Griffiths, L. J. and D. J. Martin. 1974. "A Study of the Dynamic Behaviour of a Carbon-Fiber Composite Using the Split Hopkinson Pressure Bar," *J. Phys. D: Appl. Phys.*, 7:2329–2341.
20. Bai, Y. and J. Harding. 1984. "Fracture Initiation in Glass-Reinforced Plastics under Impact Compression," in *Proceedings of International Conference on Structural Impact and Crashworthiness.* London: Imperial College, 2:482–493.
21. Walley, S. M., J. E. Field, P. H. Pope and N. A. Safford. 1989. "A Study of the Rapid Deformation Behaviour of a Range of Polymers," *Phil. Trans. R. Soc. Lond.*, A328:1–33.
22. Harding, J. and L. M. Welsh. 1983. "A Tensile Testing Technique for Fiber-Reinforced Composites at Impact Rates of Strain," *J. Mater. Sci.*, 18:1810–1826.
23. Harding, J., Y. Li, K. Saka and M. E. C. Taylor. 1989. "Characterisation of the Impact Strength of Woven Carbon/Epoxy Laminates," in *Proceedings of the 4th Oxford Conference on Mechanical Properties of Materials at High Rates of Strain.* Institute of Physics, pp. 403–410.
24. Saka, K. and J. Harding. 1990. "A Simple Laminate Theory Approach to the Prediction of the Tensile Impact Strength of Woven Hybrid Composites," *Composites*, 21:439–447.
25. Li, R. K. Y., Y. M. Wong and J. Harding. 1992. "Strain Rate Effect on the Elastic Properties of PPS (Polyphenylene Sulfide) Composites," in *Proceedings of the 2nd International Symposium on Composite Materials and Structures.* Peking University Press, pp. 25–30.
26. Chiem, C. Y. and Z. G. Liu. 1988. "The Relationship between Tensile Strength and Shear Strength in Composite Materials Subjected to High Strain Rates," *J. of Engineering Materials and Technology*, 110:191–194.
27. Sawyer, L. C. and M. Jaffe. 1986. "The Structure of Thermotropic Copolyesters," *J. Mater. Sci.*, 21:1897–1913.